

Unconventional hybrid-order topological insulators

Wei Jia,^{1,*} Yuping Tian,² Huanhuan Yang,^{3,†} Xiangru Kong,^{2,‡} Zhi-Hao Huang,⁴ Wei-Jiang Gong,² and Jun-Hong An¹

¹*Lanzhou Center for Theoretical Physics, Key Laboratory of Theoretical Physics of Gansu Province, Key Laboratory of Quantum Theory and Applications of MoE,*

Gansu Provincial Research Center for Basic Disciplines of Quantum Physics, Lanzhou University, Lanzhou 730000, China

²*College of Sciences, Northeastern University, Shenyang 110819, China*

³*Advanced Institute for Material Research (WPI-AIMR),*

Tohoku University, 2-1-1 Katahira, Sendai, 980-8577, Japan

⁴*Department of Physics, Fudan University, Shanghai 200433, China*

Exploring topological matters with exotic quantum states can update the understanding of topological phases and broaden the classification of topological materials. Here, we report a class of unconventional hybrid-order topological insulators (HyOTIs), which simultaneously host various different higher-order topological states in a single d -dimensional (d D) system. Such topological states exhibit a unique bulk-boundary correspondence that is different from first-order topological states, higher-order topological states, and the coexistence of both. Remarkably, we develop a generic surface theory to precisely capture them and firstly discover a 3D unconventional HyOTI protected by inversion symmetry, which renders both second-order (helical) and third-order (corner) topological states in one band gap and exhibits a novel bulk-edge-corner correspondence. By adjusting the parameters of the system, we also observe the nontrivial phase transitions between the inversion-symmetric HyOTI and other conventional phases. We further propose a circuit-based experimental scheme to detect these interesting results. Particularly, we demonstrate that a modified tight-binding model of bismuth can support the unconventional HyOTI, suggesting a possible route for its material realization. This work shall significantly advance the research of hybrid topological states in both theory and experiment.

Introduction.—Topological materials have always attracted great attention owing to their profound implications in fundamental physics and their promising potential for applications in quantum technologies [1–5]. The first-order and higher-order topological insulators [6–14], as the prominent examples of topological materials, have demonstrated that a d -dimensional (d D) system can host n th-order topological states in its $(d - n)$ D boundaries [15–27]. However, this understanding that a single system only emerges one type of topological order has been broken by the discovery of hybrid-order topological insulators (HyOTIs) [28–30]. Such systems allow that first-order and second-order topological states coexist in the same or different band gaps, which have been experimentally observed in a 2D phononic crystal [31] and a 3D realistic solid arsenic [32].

To date, a general perspective holds that the HyOTIs only allow the coexistence of both first-order and higher-order topological states [33–36]. It is important that the HyOTIs in higher dimensional systems ($d \geq 3$), by their fundamental nature, may exhibit the coexistence of topological states across multiple orders. This implies that a single d D system may simultaneously host various different higher-order topological states, i.e., the unconventional HyOTI, which can drive the novel bulk-boundary correspondence that is different from the conventional one and extend the classification of topological materials. But it has never been reported. On the other hand, if the unconventional HyOTIs exist, a critical issue is how to effectively identify and exactly characterize them, as these

nontrivial states extend beyond the basic description of first-order, higher-order, and conventional hybrid-order topological states (coexistence of first-order and higher-order topological states).

In this Letter, we reveal a class of unconventional HyOTIs, which can simultaneously host various different higher-order topological states in a d D gapped system. We further employ the effective mass fields on $(d - 1)$ D real-space surfaces to construct a set of topological indices, whose nonzero values provide the precise determination of their orders. By applying this theory, we discover a 3D inversion-symmetric unconventional HyOTI, which hosts both helical and corner topological states in a single band gap. Such HyOTI is characterized by a \mathbb{Z}_2 topological invariant, manifesting as a bulk-edge-corner correspondence. Particularly, the conventional HyOTI, second-order topological insulators (SOTIs), and Weyl semimetals are also observed by adjusting the parameters of the system, with which the nontrivial phase transitions emerge between the inversion-symmetric HyOTI and them. We further propose a circuit-based scheme to detect these special properties. Finally, we predict that a modified tight-binding model of bismuth can support the inversion-symmetric unconventional HyOTI, providing an insight to seek its material candidate.

Generic surface theory.—Our starting point is a d D topological insulator hosting s th-order topological states on $(d - s)$ D boundaries. Here s takes two or more elements in the set $S = \{2, 3, \dots, n\}$ with $3 \leq n \leq d$, implying that the different higher-order topological states

can coexist in such system. The corresponding effective Hamiltonian with the boundaries reads

$$\mathcal{H}(\mathbf{k}, \mathbf{r}) = \sum_{i=1}^d k_i \gamma_i + m_{1,\mathbf{r}} \Gamma_1 + \sum_{j=2}^n m_{j,\mathbf{r}} \Gamma_j. \quad (1)$$

Here γ and Γ are the pseudospin operators and obey the anticommutation relations [37, 38], which implies that $\mathcal{H}(\mathbf{k}, \mathbf{r})$ is a Dirac-type Hamiltonian. It is observed that $\mathcal{H}(\mathbf{k}, \mathbf{r})$ consists of three parts, of which the first part is \mathbf{k} -dependent linear dispersions to characterize the properties of Dirac cones. The remaining two parts are mass terms, allowing the position \mathbf{r} dependence and are utilized to open energy gap of the Dirac cones, where $m_{1,\mathbf{r}}$ and $m_{j,\mathbf{r}}$ can be regarded as the effective bulk mass and boundary masses, respectively. We further assume $m_{1,\mathbf{r}} > 0$ ($m_{1,\mathbf{r}} < 0$) inside (outside) the topological insulator, and thus there are $m_{1,\mathbf{r}} = 0$ and $m_{j,\mathbf{r}} \neq 0$ on the $(d-1)$ D boundaries, inducing a nonzero edge energy gap. This means that the different higher-order topological states can coexist in $(d-s)$ D boundaries with $s \geq 2$, manifesting as the unconventional HyOTIs.

To exactly capture these hybrid topological states, we next study the $(d-1)$ D boundary physics of the above system. By projecting the above effective Hamiltonian to the boundaries as $\mathcal{H}(\mathbf{k}, \mathbf{r}) = \mathbf{P}(\mathbf{r})\mathcal{H}(\mathbf{k}, \mathbf{r})\mathbf{P}(\mathbf{r})$ [39–46], where $\mathbf{P}(\mathbf{r}) = [1 - i(\mathbf{n}_\mathbf{r} \cdot \gamma)\Gamma_1]/2$ denotes the projection operator to the boundaries and $\mathbf{n}_\mathbf{r}$ is the surface normal vector at the position \mathbf{r} , we obtain an effective $(d-1)$ D boundary Hamiltonian

$$\tilde{\mathcal{H}}(\mathbf{k}, \mathbf{r}) = \mathbf{k}_b \cdot \tilde{\gamma} + \sum_{j=2}^n m_{j,\mathbf{r}} \tilde{\Gamma}_j, \quad (2)$$

where $\mathbf{k}_b = \mathbf{k} - (\mathbf{k} \cdot \mathbf{n}_\mathbf{r})\mathbf{n}_\mathbf{r}$ is the boundary momentum. Here $\tilde{\gamma}$ and $\tilde{\Gamma}$ are the boundary-projected Gamma matrices, which still obey the anticommutation relations. It is seen that there are $n-1$ effective boundary masses $m_{j,\mathbf{r}}$, where $j = 2, 3, \dots, n$. When the system presents a HyOTI with $(d-s)$ D topological states, these effective boundary masses shall host q mass fields for each order s , say $\mathbf{m}_\mathbf{r}^{(s,q)} = m_{j',\mathbf{r}}$, to induce mass defects with the dimension $d_{\text{defect}} = d-s$. Here j' takes $s-1$ elements in the set S and we have $q = 1, 2, \dots, \mathbb{C}_{n-1}^{s-1}$ with \mathbb{C} being combination. Since $|\mathbf{m}_\mathbf{r}^{(s,q)}|$ is nonzero everywhere, we can define q unit mass fields as $\mathbf{M}_\mathbf{r}^{(s,q)} = \mathbf{m}_\mathbf{r}^{(s,q)} / |\mathbf{m}_\mathbf{r}^{(s,q)}|$. It is clear that $\mathbf{M}_\mathbf{r}^{(s,q)}$ is homotopic to a $(s-2)$ D sphere S^{s-2} . By further defining \mathbf{r} as a real-space parameter on S^{d_r} to surround the mass defects with codimension $d_c = (d-1) - d_{\text{defect}}$, the homotopy group $\pi_{s-2}(S^{d_r}) = \mathbb{Z}$ characterizes these mass defects [47–49]. Here $d_r = d_c - 1$ is associated with the codimension of mass defects in $(d-1)$ D boundaries. Then, we define a set of \mathbb{Z} topological invariants, say $\mathcal{V}_s^{(q)}$, to describe these mass defects, which is a $(s-2)$ D winding number $w_{s-2}^{(q)}$ for the odd s

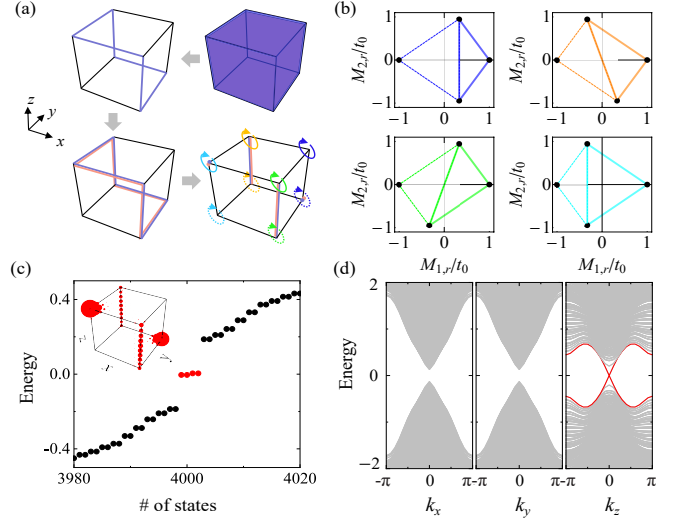


FIG. 1. (a) The generation mechanism of a 3D inversion-symmetric unconventional HyOTI in a cubic crystal. (b) The distribution of unit mass fields enclosing 8 corners of (a). The bottom right and top left corners host the mass defects, giving the nonzero $w_1^{(1)}$ and driving the corner states. The front and back edges host the mass defects, giving the nonzero $C_0^{(1),(2)}$ and driving the helical states. (c)-(d) The OBC energy spectrum gives four zero-energy states located in corners and hinges. The lattice size is $10 \times 10 \times 10$. The other parameters are $m_0 = t_0$ and $B_0 = 0.35t_0$.

or the $\frac{s-2}{2}$ th Chern number $C_{\frac{s-2}{2}}^{(q)}$ for the even s [38], i.e.,

$$\mathcal{V}_s^{(q)} = \begin{cases} w_{s-2}^{(q)}, & s-2 \in \text{odd}, \\ C_{\frac{s-2}{2}}^{(q)}, & s-2 \in \text{even}. \end{cases} \quad (3)$$

Hence, these nonzero $\mathcal{V}_s^{(q)}$ provide an elegant way to determine the orders s of the unconventional HyOTI. Besides, it is noted that this surface theory is also applicable for the dD non-Dirac bulk Hamiltonian, as soon as its $(d-1)$ D effective boundary Hamiltonian is Dirac-type, i.e., it is similar to Eq. (2).

3D inversion-symmetric HyOTI.—Inspired by the surface theory, we discover a 3D inversion-symmetric unconventional HyOTI in a cubic crystal, with the coexistence of helical and corner states. The corresponding momentum-space Hamiltonian reads

$$\mathcal{H}(\mathbf{k}) = \sum_{i=1}^3 h_i \gamma_i + h_4 \Gamma_1 + \sum_{i=1}^3 B_0 \Gamma_{i+1} + h_5 \Gamma_5, \quad (4)$$

where h -components are given by $h_i = t_0 \sin k_i$, $h_4 = [m_0 - t_0(3 - \sum_{i=1}^3 \cos k_i)]$, and $h_5 = t_0(\cos k_1 - \cos k_2)$. Here t_0 and B_0 are \mathbf{k} -independent constants and we take $k_{1,2,3} = k_{x,y,z}$. The Gamma matrices are $\gamma_1 = \rho_3 \tau_1 \sigma_1$, $\gamma_2 = \rho_3 \tau_1 \sigma_2$, $\gamma_3 = \rho_3 \tau_1 \sigma_3$, $\Gamma_1 = \rho_3 \tau_3$, $\Gamma_2 = \rho_3 \sigma_1$, $\Gamma_3 = \rho_3 \sigma_2$, $\Gamma_4 = \rho_3 \sigma_3$, and $\Gamma_5 = \rho_2$, where the Pauli matrices σ_i , τ_i , and ρ_i denote the freedom degree of spin,

orbit, and sublattice, respectively. Note that $\mathcal{H}(\mathbf{k})$ only presents the inversion symmetry with $\mathcal{I} = \tau_3$ and is a non-Dirac type Hamiltonian due to $[\Gamma_{i+1}, \gamma_i] = 0$ and $[\Gamma_{2,3,4}, \Gamma_1] = 0$ with $i = 1, 2, 3$.

Physically, the 3D inversion-symmetric HyOTI can be understood through four processes, as shown in Fig. 1(a). Firstly, we consider a 3D traditional \mathbb{Z}_2 topological insulator, described by $\mathcal{H}_0(\mathbf{k}) = h_4\tau_3 + \sum_{i=1}^3 h_i\tau_1\sigma_i$ [15]. In addition to $\mathcal{I} = \tau_3$, the system also presents time-reversal symmetry $\mathcal{T} = i\sigma_2\mathcal{K}$ and four-fold rotation symmetry $C_4 = e^{-i\pi\sigma_3/4}$, which protect the existence of 2D surface states. Secondly, we add a magnetic field \mathbf{B} in the \mathbb{Z}_2 topological insulator, which induces the system to arrive $\mathcal{H}_0(\mathbf{k}) + \mathcal{H}_1(\mathbf{k})$, with $\mathcal{H}_1(\mathbf{k}) = \sum_{i=1}^3 B_i\sigma_i$ and $B_i = B_0$. The nonzero \mathbf{B} breaks \mathcal{T} and C_4 , thereby opening the energy gap of all surface states. Since \mathcal{I} is still preserved and the surfaces perpendicular to \mathbf{r} and $-\mathbf{r}$ have opposite magnetic flux, the chiral hinge states are emerged in the edges intersected by these surfaces [50]. Thirdly, we perform the time-reversal copy for the above system with chiral hinge states. Then, it is described by $\rho_3[\mathcal{H}_0(\mathbf{k}) + \mathcal{H}_1(\mathbf{k})]$, which drives these chiral hinge states to helical states. Finally, we add $\mathcal{H}_2(\mathbf{k}) = h_5\rho_2$ to open the energy gap of helical states on (001) and $(00\bar{1})$ surfaces, which induces the corner states. As $\mathcal{H}_2(\mathbf{k})$ is independent to k_z and preserves the helical states along z direction, we obtain the unconventional HyOTI with helical and corner states, as shown in Fig. 1(a).

The surface theory further illustrates that the Hamiltonian (4) can exhibit the HyOTI. By using the operator $\mathbf{P}(\mathbf{r}) = [1 - i(\mathbf{n}_r \cdot \boldsymbol{\gamma})\Gamma_1]/2$ to project $\mathcal{H}(\mathbf{k})$ into six 2D surfaces of a cubic crystal, the effective surface Hamiltonians are easily obtained [51]. We examine their unit mass fields \mathbf{M}_r surrounding 8 corners and 16 edges [see Figs. 1(a) and 1(b)]. For the corner intersected by (001) , $(0\bar{1}0)$, and $(\bar{1}00)$ surfaces, these unit mass fields contribute $w_1^{(1)} = 1$ in the parameter space of enclosing this corner. Then, we identify that there are 0D topological states in this corner. For the edge intersected by (100) and $(0\bar{1}0)$ surfaces, these unit mass fields contribute $C_0^{(1)} = C_0^{(2)} = 1$. Thus, there are 1D topological states in this edge. Similarly, the remaining edges and corners are also identified, showing that this system simultaneously host second-order and third-order topological states [51]. Furthermore, we numerically obtain the energy spectrum of $\mathcal{H}(\mathbf{k})$ under open boundary conditions (OBCs), as shown in Figs. 1(c) and 1(d). It is seen that the helical states are located at two edges along z direction and the corner states are located at one corner of the other two edges, which completely matches with the previous results of surface theory.

Topological phase diagram.—The band structure of this 3D inversion-symmetric HyOTI can be obtained by diagonalizing the Hamiltonian $\mathcal{H}(\mathbf{k})$. It allows that the phase boundaries of system are determined by closing

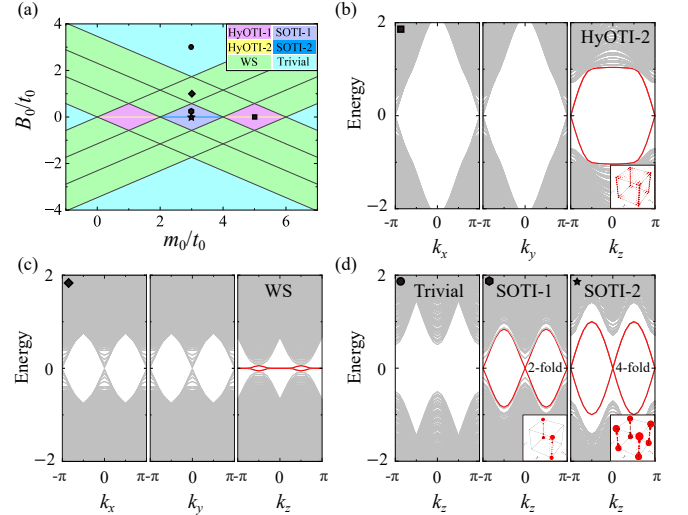


FIG. 2. Topological phase diagram of the model (4), including HyOTI-1, HyOTI-2, SOTI-1, SOTI-2, WS, and trivial phases. The OBC energy spectra are shown in (b) HyOTI-2, (c) WS, and (d) trivial phase, SOTI-1, and SOTI-2. The insets give the distribution of zero-energy states. Here the parameters are $m_0 = 5t_0$ and $B_0 = 0$ for (b), $m_0 = 3t_0$ and $B_0 = t_0$ for (c), $m_0 = 3t_0$ and $B_0 = 3t_0, 0.35t_0$, and 0 for (d).

bulk energy gap at four high-symmetry points $\mathbf{D}_1 = (0, 0, 0)$, $\mathbf{D}_2 = (0, 0, -\pi)$, $\mathbf{D}_3 = (-\pi, -\pi, 0)$, and $\mathbf{D}_4 = (-\pi, -\pi, -\pi)$. Namely, the phase transitions occur at $\sqrt{3}B_0 = \pm m_0, \pm(m_0 - 2t_0), \pm(m_0 - 4t_0)$, and $\pm(m_0 - 6t_0)$. Moreover, the phase transitions can emerge from $B_0 = 0$ to $B_0 \neq 0$ due to the change of symmetries, although the bulk energy gap is kept. With this, we obtain the topological phase diagram in Fig. 2(a). It is observed that there are six different phases: (i) unconventional HyOTI with two-fold helical and corner states (HyOTI-1); (ii) conventional HyOTI with four-fold helical states and xy -surface states (HyOTI-2); (iii) Weyl semimetal (WS); (iv) trivial phase; (v) SOTI with two-fold helical states (SOTI-1); (vi) SOTI with four-fold helical states (SOTI-2). By adjusting the strength of magnetic field, these phases render rich transitions. Particularly, there are two exotic types have not been reported so far, where one occurs between WS and HyOTI-1 by closing bulk energy gap, and the other occurs between HyOTI-1 and HyOTI-2 by changing the symmetries.

Besides, the above topological phase diagram implies that HyOTI-1 is induced by HyOTI-2, when changing the magnetic field B_0 from zero to nonzero. It allows that the topological characterization of HyOTI-2 is extended to HyOTI-1. Given that the inversion symmetry is always presented, we define a \mathbb{Z}_2 topological index

$$\nu = \frac{\nu_+ - \nu_-}{2} \bmod 2 \quad (5)$$

to characterize both HyOTI-1 and HyOTI-2. Here ν_\pm are defined by $\mathcal{H}_\pm(\mathbf{k})$ which acts on the inversion subspace

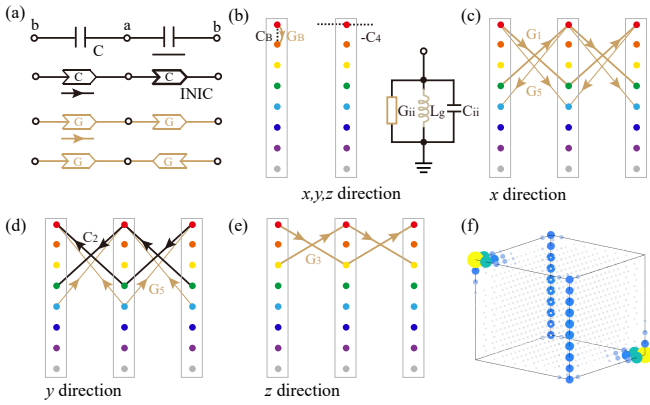


FIG. 3. (a) General circuit models for realizing distinct interactions. Here, INIC unit acts as a positive (negative) capacitor/resistor from right to left (left to right). (b) Circuit implementation of the magnetic field terms (left), hopping term h_4 (middle), and on-site potentials (right). (c)-(e) Other hopping terms along the x , y , and z directions for first node. (f) Numerical impedance of a finite-size circuit model.

with even (+) and odd (−) parity, respectively. Since the rotoinversion symmetry with $\bar{C}_4 = C_4\mathcal{I}$ are emerged for $\mathcal{H}_{\pm}(\mathbf{k})$ at $B_0 = 0$, we have

$$\nu_{\pm} = \frac{1}{2\sqrt{2}} \sum_{\mathbf{K}} \sum_{\alpha} e^{\frac{i\alpha\pi}{4}} n_{\mathbf{K}}^{\alpha, \pm}. \quad (6)$$

Here \mathbf{K} runs over the points $\mathbf{D}_{1,2,3,4}$ and $n_{\mathbf{K}}^{\alpha, \pm}$ is the number of the occupied bands of $\mathcal{H}_{\pm}(\mathbf{k})$ with the eigenvalue $e^{\frac{i\alpha\pi}{4}}$ of the operator \bar{C}_4 [52]. After some straightforward calculations, we have $\nu = 1$ for both HyOTI-1 and HyOTI-2, while $\nu = 0$ is for the other phases. These results reveal a unique bulk-edge-corner (bulk-surface-edge) correspondence in HyOTI-1 (HyOTI-2).

Circuit-based realization.—Topological circuits constitute a versatile platform for simulating lattice Hamiltonians with nontrivial band topology [53–56]. Here, we realize the inversion-symmetric HyOTI by mapping the Bloch Hamiltonian (4) onto a frequency-dependent circuit Laplacian, i.e., $\mathcal{H}(\mathbf{k}) \rightarrow -i\mathcal{J}(\omega)$, following Refs.[57, 58]. To reproduce the distinct hopping amplitudes in $\mathcal{H}(\mathbf{k})$, we employ the general circuit cell shown in Fig. 3(a). For an infinitely extended chain its admittance elements are $j_{ab} = i[-2\omega C \cos k]$, $j_{ab} = i[2i\omega C \sin k]$, $j_{ab} = i[2G \sin k]$, and $j_{ab} = i[2iG \cos k]$, respectively, where C (G) denotes the capacitance (conductance) and k is the momentum along the chain.

Using these building blocks we construct a 3D cubic network whose unit cell contains 8 circuit nodes connected by capacitors (C), inductors (L), resistors ($R = 1/G$), and negative impedance converter with current inversion (INICs), as sketched in Figs. 3(b)–(e). For clarity, only the couplings from the first (red) node are shown. The full 8×8 Laplacian matrix $\mathcal{J}(\omega)$, which exactly implements the Hamiltonian $\mathcal{H}(\mathbf{k})$, is given in

the Supplemental Material [51]. For a finite sample with $N_x = N_y = N_z = 10$ unit cells, we assemble the corresponding Laplacian and compute the impedance between each node and the ground numerically. The result, displayed in Fig. 3(f), exhibits simultaneous boundary resonances characteristic of second-order and third-order topological states, thereby confirming our hybrid-order theoretical framework. By further adjusting the parameters of the circuit, we can realize all the phases in Fig. 3(a) and observe these nontrivial phase transitions. This scheme provides a feasible experimental way to detect the nontrivial properties emerged in the inversion-symmetric unconventional HyOTI.

Possible material candidates.—We next show that the 3D unconventional HyOTI can be observed in a hexagonal lattice hosting the tight-binding Hamiltonian

$$\mathcal{H}_{\text{TB}}(\mathbf{k}) = \begin{bmatrix} \mathcal{H}_I(\mathbf{k}) + m_z & \delta\mathcal{M}(\mathbf{k}) + m_x \\ \delta\mathcal{M}(\mathbf{k})^\dagger + m_x & \mathcal{H}_{II}(\mathbf{k}) - m_z \end{bmatrix}. \quad (7)$$

When the additional mass terms $m_{x,z}$ vanish, it is seen that $\mathcal{H}_{\text{TB}}(\mathbf{k})$ consists of two 3D topological insulators given by $\mathcal{H}_I(\mathbf{k})$ and $\mathcal{H}_{II}(\mathbf{k})$ and they couple together via the mass matrix $\mathcal{M}(\mathbf{k})$ with the coupling strength δ [51]. Then, $\mathcal{H}_{\text{TB}}(\mathbf{k})$ is topologically equivalent to the realistic model of pure bismuth [59, 60], which renders a SOTI with helical states. The OBC energy spectrum is shown in Fig. 4(a), where 8 states marked as red contribute at the edges. We emphasize that such helical states are determined by the mass domain walls induced by effective surface masses [see the inset of Fig. 4(a)].

However, the nonzero $m_{x,z}$ can change the effective surface masses into the forms of the inset of Fig. 4(b), resulting in the unconventional HyOTI [51]. The OBC energy spectrum in Fig. 4(b) confirms that the system host both helical and corner states. Note that the forms of additional mass terms can be arbitrary, but the system can show such unconventional HyOTI as soon as the effective surface mass field meets the requirements of Eq. (3). These results shall provide a possible route to seek the realistic unconventional HyOTI in bismuth-based materials.

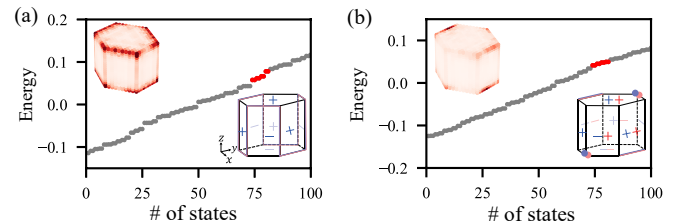


FIG. 4. The OBC energy spectrum of the tight-binding model (a) without and (b) with additional mass terms on a hexagonal structure. The 100 eigenstates near the Fermi level are plotted, where two insets illustrate the real-space contributions of the states with red color and the signs of effective surface masses, respectively. The system size is $20 \times 20 \times 20$.

Outlook.—In static and Hermitian systems, we have uncovered a class of unconventional HyOTIs, which can simultaneously host various different higher-order topological states. Actually, such hybrid topological states may also emerge in non-Hermitian and Floquet systems, as the coexistence of first-order and second-order topological states has been observed in these systems [61–65]. Moreover, the recent experiments have demonstrated that pure bismuth is a SOTI with helical states [66, 67]. We have predicted that the tight-binding model of bismuth can support the unconventional HyOTI by adjusting the relative energy shift (i.e., m_z) between two topological insulator layers and changing their coupling constant (i.e., m_x). In the realistic materials, a possible route to achieving the unconventional HyOTIs involves doping bismuth with magnetic elements [68, 69] or interfacing with magnetic substrates [70, 71]. Both of two processes can tune the effective surface masses to satisfy the requirements of the surface theory. Hence, our work provides an insight to explore novel hybrid topological states in the broader topological systems.

Acknowledgements.—We thank Dr. Zhi-Xiong Li and Prof. Xiong-Jun Liu for the helpful discussions. W. Jia is supported by the National Natural Science Foundation of China (Grant No. 12404318), the Fundamental Research Funds for the Central Universities (Grant No. lzujbky-2024-jdzx06), the Natural Science Foundation of Gansu Province (No. 22JR5RA389), and the ‘111 Center’ under Grant No. B20063. X. Kong is supported by the Fundamental Research Funds for the Central Universities (No. N25LPY025).

(2017).

- [9] Z. Song, Z. Fang, and C. Fang, (d-2)-dimensional edge states of rotation symmetry protected topological states, *Phys. Rev. Lett.* **119**, 246402 (2017).
- [10] J. Langbehn, Y. Peng, L. Trifunovic, F. von Oppen, and P. W. Brouwer, Reflection-symmetric second-order topological insulators and superconductors, *Phys. Rev. Lett.* **119**, 246401 (2017).
- [11] F. Schindler, A. M. Cook, M. G. Vergniory, Z. Wang, S. S. Parkin, B. A. Bernevig, and T. Neupert, Higher-order topological insulators, *Sci. Adv.* **4**, eaat0346 (2018).
- [12] X.-L. Sheng, C. Chen, H. Liu, Z. Chen, Z.-M. Yu, Y. X. Zhao, and S. A. Yang, Two-dimensional second-order topological insulator in graphdiyne, *Phys. Rev. Lett.* **123**, 256402 (2019).
- [13] M. Serra-Garcia, V. Peri, R. Süsstrunk, O. R. Bilal, T. Larsen, L. G. Villanueva, and S. D. Huber, Observation of a phononic quadrupole topological insulator, *Nature* **555**, 342 (2018).
- [14] C. W. Peterson, W. A. Benalcazar, T. L. Hughes, and G. Bahl, A quantized microwave quadrupole insulator with topologically protected corner states, *Nature* **555**, 346 (2018).
- [15] B. A. Bernevig, T. L. Hughes, and S.-C. Zhang, Quantum spin Hall effect and topological phase transition in HgTe quantum wells, *Science* **314**, 1757 (2006).
- [16] F. Zhang, C. L. Kane, and E. J. Mele, Surface state magnetization and chiral edge states on topological insulators, *Phys. Rev. Lett.* **110**, 046404 (2013).
- [17] M. Ezawa, Topological switch between second-order topological insulators and topological crystalline insulators, *Phys. Rev. Lett.* **121**, 116801 (2018).
- [18] R. Queiroz and A. Stern, Splitting the hinge mode of higher-order topological insulators, *Phys. Rev. Lett.* **123**, 036802 (2019).
- [19] L. Trifunovic and P. W. Brouwer, Higher-order bulk-boundary correspondence for topological crystalline phases, *Phys. Rev. X* **9**, 011012 (2019).
- [20] W. Jia, L. Zhang, L. Zhang, and X.-J. Liu, Dynamically characterizing topological phases by high-order topological charges, *Phys. Rev. A* **103**, 052213 (2021).
- [21] L. Zhang, W. Jia, and X.-J. Liu, Universal topological quench dynamics for \mathbb{Z}_2 topological phases, *Sci. Bull.* **67**, 1236 (2022).
- [22] X.-L. Yu, W. Ji, L. Zhang, Y. Wang, J. Wu, and X.-J. Liu, Quantum dynamical characterization and simulation of topological phases with high-order band inversion surfaces, *Phys. Rev. X Quantum* **2**, 020320 (2021).
- [23] L. Li, W. Zhu, and J. Gong, Direct dynamical characterization of higher-order topological phases with nested band inversion surfaces, *Sci. Bull.* **66**, 1502 (2021).
- [24] Y. Tan, Z.-H. Huang, and X.-J. Liu, Two-particle berry phase mechanism for dirac and majorana kramers pairs of corner modes, *Phys. Rev. B* **105**, L041105 (2022).
- [25] Z. Lei, Y. Deng, and L. Li, Topological classification of higher-order topological phases with nested band inversion surfaces, *Phys. Rev. B* **106**, 245105 (2022).
- [26] W. A. Benalcazar and A. Cerjan, Chiral-Symmetric Higher-Order Topological Phases of Matter, *Phys. Rev. Lett.* **128**, 127601 (2022).
- [27] W. Jia, B.-Z. Wang, M.-J. Gao, and J.-H. An, Unveiling higher-order topology via polarized topological charges, *Phys. Rev. B* **110**, L201117 (2024).
- [28] N. Bultinck, B. A. Bernevig, and M. P. Zaletel, Three-

* jiaw@lzu.edu.cn

† yang.huanhuan.b6@tohoku.ac.jp

‡ kongxiangru@mail.neu.edu.cn

- [1] K. v. Klitzing, G. Dorda, and M. Pepper, New method for high-accuracy determination of the fine-structure constant based on quantized Hall resistance, *Phys. Rev. Lett.* **45**, 494 (1980).
- [2] D. J. Thouless, M. Kohmoto, M. P. Nightingale, and M. den Nijs, Quantized hall conductance in a two-dimensional periodic potential, *Phys. Rev. Lett.* **49**, 405 (1982).
- [3] X.-G. Wen, Non-Abelian statistics in the fractional quantum Hall states, *Phys. Rev. Lett.* **66**, 802 (1991).
- [4] A. Y. Kitaev, Fault-tolerant quantum computation by anyons, *Ann. Phys.* **303**, 2 (2003).
- [5] M. Z. Hasan and C. L. Kane, Colloquium: topological insulators, *Rev. Mod. Phys.* **82**, 3045 (2010).
- [6] X.-L. Qi and S.-C. Zhang, Topological insulators and superconductors, *Rev. Mod. Phys.* **83**, 1057 (2011).
- [7] W. A. Benalcazar, B. A. Bernevig, and T. L. Hughes, Quantized electric multipole insulators, *Science* **357**, 61 (2017).
- [8] F. Liu and K. Wakabayashi, Novel topological phase with a zero berry curvature, *Phys. Rev. Lett.* **118**, 076803

- dimensional superconductors with hybrid higher-order topology, *Phys. Rev. B* **99**, 125149 (2019).
- [29] S. H. Kooi, G. Van Miert, and C. Ortix, Hybrid-order topology of weak topological insulators, *Phys. Rev. B* **102**, 041122 (2020).
- [30] X. Zhang, Z.-K. Lin, H.-X. Wang, Z. Xiong, Y. Tian, M.-H. Lu, Y.-F. Chen, and J.-H. Jiang, Symmetry-protected hierarchy of anomalous multipole topological band gaps in nonsymmorphic metacrystals, *Nat. Commun.* **11**, 65 (2020).
- [31] Y. Yang, J. Lu, M. Yan, X. Huang, W. Deng, and Z. Liu, Hybrid-order topological insulators in a phononic crystal, *Phys. Rev. Lett.* **126**, 156801 (2021).
- [32] M. S. Hossain, F. Schindler, R. Islam, Z. Muhammad, Y.-X. Jiang, Z.-J. Cheng, Q. Zhang, T. Hou, H. Chen, M. Litskevich, *et al.*, A hybrid topological quantum state in an elemental solid, *Nature* **628**, 527 (2024).
- [33] P. Lai, J. Wu, Z. Pu, Q. Zhou, J. Lu, H. Liu, W. Deng, H. Cheng, S. Chen, and Z. Liu, Real-projective-plane hybrid-order topological insulator realized in phononic crystals, *Phys. Rev. Appl.* **21**, 044002 (2024).
- [34] N.-J. Yang, Z. Huang, and J.-M. Zhang, Hybrid-order topological phase and transition in 1h transition metal compounds, *Appl. Phys. Lett.* **125** (2024).
- [35] Y.-Q. Zhu, Z. Zheng, G. Palumbo, and Z. D. Wang, Topological insulators with hybrid-order boundary states, *Phys. Rev. B* **111**, 195107 (2025).
- [36] N.-J. Yang, J.-M. Zhang, X.-P. Li, Z. Zhang, Z.-M. Yu, Z. Huang, and Y. Yao, Sliding ferroelectrics induced hybrid-order topological phase transitions, *Phys. Rev. Lett.* **134**, 256602 (2025).
- [37] T. Morimoto and A. Furusaki, Topological classification with additional symmetries from Clifford algebras, *Phys. Rev. B* **88**, 125129 (2013).
- [38] C.-K. Chiu, J. C. Y. Teo, A. P. Schnyder, and S. Ryu, Classification of topological quantum matter with symmetries, *Rev. Mod. Phys.* **88**, 035005 (2016).
- [39] W. A. Benalcazar, B. A. Bernevig, and T. L. Hughes, Electric multipole moments, topological multipole moment pumping, and chiral hinge states in crystalline insulators, *Phys. Rev. B* **96**, 245115 (2017).
- [40] Y. Hwang, J. Ahn, and B.-J. Yang, Fragile topology protected by inversion symmetry: Diagnosis, bulk-boundary correspondence, and wilson loop, *Phys. Rev. B* **100**, 205126 (2019).
- [41] Z. Yan, Higher-order topological odd-parity superconductors, *Phys. Rev. Lett.* **123**, 177001 (2019).
- [42] R.-X. Zhang, W. S. Cole, and S. Das Sarma, Helical hinge majorana modes in iron-based superconductors, *Phys. Rev. Lett.* **122**, 187001 (2019).
- [43] L. Trifunovic and P. W. Brouwer, Higher-Order Topological Band Structures, *Phys. Status Solidi B* **258**, 2000090 (2021).
- [44] L. Zhang and X.-J. Liu, Unconventional floquet topological phases from quantum engineering of band-inversion surfaces, *PRX Quantum* **3**, 040312 (2022).
- [45] W. Jia, X.-C. Zhou, L. Zhang, L. Zhang, and X.-J. Liu, Unified characterization for higher-order topological phase transitions, *Phys. Rev. Res.* **5**, L022032 (2023).
- [46] Z.-H. Huang, Y. Tan, W. Jia, L. Zhang, and X.-J. Liu, Surface chern-simons theory for third-order topological insulators and superconductors, *arXiv:2403.00316* (2024).
- [47] J. C. Teo and C. L. Kane, Topological defects and gapless modes in insulators and superconductors, *Phys. Rev. B* **82**, 115120 (2010).
- [48] K. Shiozaki and M. Sato, Topology of crystalline insulators and superconductors, *Phys. Rev. B* **90**, 165114 (2014).
- [49] M. Geier, L. Trifunovic, M. Hoskam, and P. W. Brouwer, Second-order topological insulators and superconductors with an order-two crystalline symmetry, *Phys. Rev. B* **97**, 205135 (2018).
- [50] E. Khalaf, Higher-order topological insulators and superconductors protected by inversion symmetry, *Phys. Rev. B* **97**, 205136 (2018).
- [51] See Supplemental Material for the details: (I) Effective surface Hamiltonians of inversion-symmetric HyOTI in a cubic crystal. (II) More applications of surface theory. (III) The circuit-based scheme for the inversion-symmetric HyOTIs. (IV) The completely numerical results of tight-binding model of bismuth with additional mass terms. The Supplemental Material has included Refs. [59, 60, 66].
- [52] E. Khalaf, H. C. Po, A. Vishwanath, and H. Watanabe, Symmetry indicators and anomalous surface states of topological crystalline insulators, *Phys. Rev. X* **8**, 031070 (2018).
- [53] W. Zhang, D. Zou, Q. Pei, W. He, J. Bao, H. Sun, and X. Zhang, Experimental observation of higher-order topological anderson insulators, *Phys. Rev. Lett.* **126**, 146802 (2021).
- [54] Y. Wang, H. M. Price, B. Zhang, and Y. Chong, Circuit implementation of a four-dimensional topological insulator, *Nat. Comm.* **11**, 2356 (2020).
- [55] R. Yu, Y. Zhao, and A. P. Schnyder, 4d spinless topological insulator in a periodic electric circuit, *Nat. Sci. Rev.* **7**, 1288 (2020).
- [56] L. Qian, W. Zhang, H. Sun, and X. Zhang, Non-abelian topological bound states in the continuum, *Phys. Rev. Lett.* **132**, 046601 (2024).
- [57] T. Helbig, T. Hofmann, S. Imhof, M. Abdelghany, T. Kiessling, L. Molenkamp, C. Lee, A. Szameit, M. Greiter, and R. Thomale, Generalized bulk-boundary correspondence in non-hermitian topolectrical circuits, *Nat. Phys.* **16**, 747 (2020).
- [58] H. Yang, L. Song, Y. Cao, and P. Yan, Circuit realization of topological physics, *Phys. Rep.* **1093**, 1 (2024).
- [59] Y. Liu and R. E. Allen, Electronic structure of the semimetals bi and sb, *Phys. Rev. B* **52**, 1566 (1995).
- [60] Y. Ohtsubo and S.-i. Kimura, Topological phase transition of single-crystal bi based on empirical tight-binding calculations, *New J. Phys.* **18**, 123015 (2016).
- [61] W. Sun, L. Luo, Y. Huang, J. Peng, D. Zhao, Y. Yao, F. Wu, and X. Zhang, Observation of acoustic hybrid-order topological insulator induced by non-hermiticity and anisotropy, *Phys. Rev. B* **109**, 134302 (2024).
- [62] J. Wu, Y. Hu, Z. He, K. Deng, X. Huang, M. Ke, W. Deng, J. Lu, and Z. Liu, Hybrid-order skin effect from loss-induced nonreciprocity, *Phys. Rev. Lett.* **134**, 176601 (2025).
- [63] C. H. Lee, L. Li, and J. Gong, Hybrid higher-order skin-topological modes in nonreciprocal systems, *Phys. Rev. Lett.* **123**, 016805 (2019).
- [64] H. Wu and J.-H. An, Hybrid-order topological odd-parity superconductors via floquet engineering, *Phys. Rev. B* **107**, 235132 (2023).
- [65] H. Wu, Y.-C. Dong, and H. Liu, Floquet topological

- phases with time-reversal and space-inversion symmetries and dynamical detection of topological charges, *Phys. Rev. B* **110**, 235140 (2024).
- [66] F. Schindler, Z. Wang, M. G. Vergniory, A. M. Cook, A. Murani, S. Sengupta, A. Y. Kasumov, R. Deblock, S. Jeon, I. Drozdov, H. Bouchiat, S. Guéron, A. Yazdani, B. A. Bernevig, and T. Neupert, Higher-order topology in bismuth, *Nat. Phys.* **14**, 918 (2018).
 - [67] D. Zhao, Y. Zhong, T. Yuan, H. Wang, T. Jiang, Y. Qi, H. Xiang, X. Gong, D. Feng, and T. Zhang, Revealing higher-order topological bulk-boundary correspondence in bismuth crystal with spin-helical hinge state loop and proximity superconductivity, *arXiv:2502.07533* (2025).
 - [68] P. Hofmann, The surfaces of bismuth: Structural and electronic properties, *Prog. Surf. Sci.* **81**, 191 (2006).
 - [69] G. S. Hegde and A. Prabhu, A review on doped/composite bismuth chalcogenide compounds for thermoelectric device applications: various synthesis techniques and challenges, *J. Electron. Mater.* **51**, 2014 (2022).
 - [70] D. Li, S. Haldar, T. Drevelow, and S. Heinze, Tuning the magnetic interactions in van der waals Fe_3GeTe_2 heterostructures: A comparative study of ab initio methods, *Phys. Rev. B* **107**, 104428 (2023).
 - [71] X. Zhou, W. Feng, Y. Li, and Y. Yao, Spin-chirality-driven quantum anomalous and quantum topological hall effects in chiral magnets, *Nano Lett.* **23**, 5680 (2023).

Supplementary Material for “Unconventional hybrid-order topological insulators”

In this Supplementary Material, we provide the details of effective surface Hamiltonians in Sec. I. We show the more applications of the surface theory in Sec. II. We also provide the details of circuit-based scheme for the inversion-symmetric HyOTIs in Sec. III. We finally show the completely numerical results of the tight-binding model of bismuth with additional mass terms in Sec. IV.

I. Surface Hamiltonians in a cubic geometry

We consider a general momentum-space Hamiltonian, which can host 3D inversion-symmetric HyOTI with helical and corner states in a cubic crystal. It is written as

$$\mathcal{H}(\mathbf{k}) = \left[m_0 - t_0 \left(3 - \sum_{i=1}^3 \cos k_i \right) \right] \rho_3 \tau_3 \sigma_0 + t_0 \sum_{i=1}^3 \sin k_i \rho_3 \tau_1 \sigma_i + \sum_{i=1}^3 B_i \rho_3 \tau_0 \sigma_i + t_0 (\cos k_1 - \cos k_2) \rho_2 \tau_0 \sigma_0. \quad (\text{S1})$$

Here the Pauli matrices σ_i , τ_i , and ρ_i denote the freedom degree of spin, orbit, and sublattice, respectively. Note that ρ_0 , τ_0 , and σ_0 are identity matrices. This Bloch Hamiltonian $\mathcal{H}(\mathbf{k})$ is same with Eq. (5) of the main text when taking $B_{1,2,3} = B_0$. We obtain its low-energy effective Hamiltonian as follows:

$$\mathcal{H}_{\text{eff}}(\mathbf{k}) = \left[m_0 - t_0 \left(\frac{1}{2}k_1^2 + \frac{1}{2}k_2^2 + \frac{1}{2}k_3^2 \right) \right] \rho_3 \tau_3 \sigma_0 + t_0 \sum_i k_i \rho_3 \tau_1 \sigma_i + \sum_i B_i \rho_3 \tau_0 \sigma_i + t_0 \left(\frac{1}{2}k_2^2 - \frac{1}{2}k_1^2 \right) \rho_2 \tau_0 \sigma_0. \quad (\text{S2})$$

After using the projection operator $\mathbf{P}_i = (1 - i\rho_3 \tau_3 \sigma_0 \cdot \rho_3 \tau_1 \sigma_i)/2$ in the eigenspace of $i\rho_3 \tau_3 \sigma_0 \cdot \rho_3 \tau_1 \sigma_i = -1$ and projecting $\mathcal{H}_{\text{eff}}(\mathbf{k})$ along k_i with $i = 1, 2, 3$, we obtain six effective surface Hamiltonians in a cubic geometry,

$$\begin{aligned} \tilde{\mathcal{H}}_{(001)} &= \tilde{\mathcal{H}}_I(k_1, k_2) = t_0 k_1 \rho_3 \sigma_3 - t_0 k_2 \rho_3 \sigma_1 + B_3 \rho_3 \sigma_2, \\ \tilde{\mathcal{H}}_{(010)} &= \tilde{\mathcal{H}}_{II}(k_1, k_3) = t_0 k_1 \rho_3 \sigma_3 + t_0 k_3 \rho_3 \sigma_1 + B_2 \rho_3 \sigma_2 - m_0 \rho_2 \sigma_0, \\ \tilde{\mathcal{H}}_{(100)} &= \tilde{\mathcal{H}}_{III}(k_2, k_3) = -t_0 k_2 \rho_3 \sigma_3 + t_0 k_3 \rho_3 \sigma_1 + B_1 \rho_3 \sigma_2 + m_0 \rho_2 \sigma_0, \\ \tilde{\mathcal{H}}_{(00\bar{1})} &= \tilde{\mathcal{H}}_{IV}(k_1, k_2) = -t_0 k_1 \rho_3 \sigma_3 + t_0 k_2 \rho_3 \sigma_1 - B_3 \rho_3 \sigma_2, \\ \tilde{\mathcal{H}}_{(0\bar{1}0)} &= \tilde{\mathcal{H}}_V(k_1, k_3) = -t_0 k_1 \rho_3 \sigma_3 - t_0 k_3 \rho_3 \sigma_1 - B_2 \rho_3 \sigma_2 - m_0 \rho_2 \sigma_0, \\ \tilde{\mathcal{H}}_{(\bar{1}00)} &= \tilde{\mathcal{H}}_{VI}(k_2, k_3) = t_0 k_2 \rho_3 \sigma_3 - t_0 k_3 \rho_3 \sigma_1 - B_1 \rho_3 \sigma_2 + m_0 \rho_2 \sigma_0. \end{aligned} \quad (\text{S3})$$

Note that these surface Hamiltonians have been rotated without changing their topologies, so that the effective surface mass fields are easily obtained as follows:

$$\begin{aligned} \mathbf{m}_{(001)} &= (B_3, 0), & \mathbf{m}_{(010)} &= (B_2, -m_0), & \mathbf{m}_{(100)} &= (B_1, m_0), \\ \mathbf{m}_{(00\bar{1})} &= (-B_3, 0), & \mathbf{m}_{(0\bar{1}0)} &= (-B_2, -m_0), & \mathbf{m}_{(\bar{1}00)} &= (-B_1, m_0). \end{aligned} \quad (\text{S4})$$

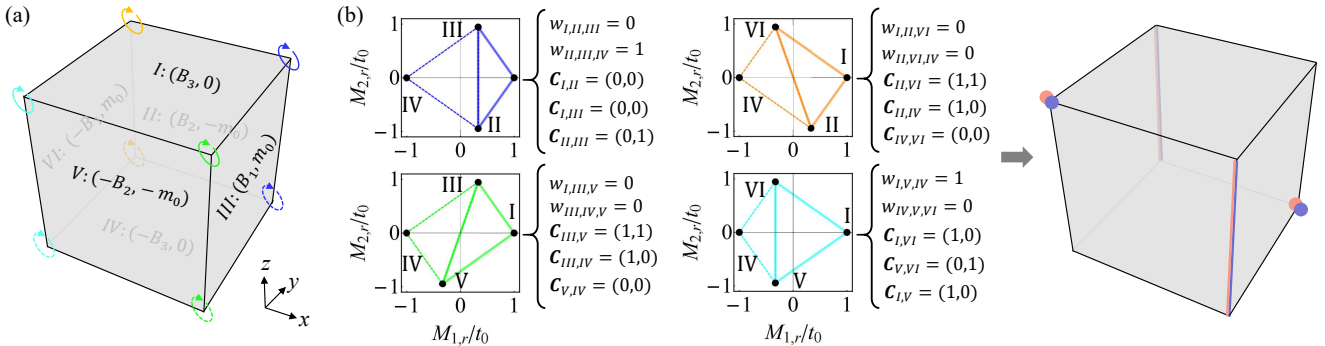


FIG. S1. (a) Distribution of effective masses on 6 surfaces of a cubic crystal. (b) A 3D unconventional HyOTI with corner and helical states can be identified by the nonzero $w_1^{(1)}$ and $C_0^{(1),(2)}$, respectively. These topological invariants are defined by the unit surface mass fields \mathbf{M}_r .

Here the subscripts of \mathbf{m} denote the Miller index. We show these effective mass fields in a cubic geometry, as shown in Fig. S1(a), where each surface hosts two effective masses. Due to the inversion symmetry, we can see that the surfaces I, II, and III (i.e., B_i) have opposite magnetic flux with the surfaces IV, V, and VI (i.e., $-B_i$).

II. More applications of the surface theory

We next provides more applications of the surface theory for the Hamiltonians (S3). To analyze the existence of topological states, the surface theory should be applied to all 8 corners and 12 edges of the cubic crystal. We first take the parameters $B_{1,2,3} = 0.35t_0$ and $m_0 = t_0$ of the main text, which actually gives a 3D inversion-symmetric HyOTI with helical and corner states. Then, the unit mass fields surrounding all 8 corners (12 edges) are numerically calculated by $\mathbf{M}_{\mathbf{r}}^{(3,1)} = (M_{1,\mathbf{r}}, M_{2,\mathbf{r}})$ [$\mathbf{M}_{\mathbf{r}}^{(2,1)} = M_{1,\mathbf{r}}$ and $\mathbf{M}_{\mathbf{r}}^{(2,2)} = M_{2,\mathbf{r}}$], as shown in Fig. S1(b), where the topological invariants of $w_1^{(1)}$ [$C_0^{(1),(2)}$] are given for these corners (edges). For example of the corner intersected by (001) , $(0\bar{1}0)$, and $(\bar{1}00)$ surfaces (i.e., the corner intersected by I, V, and VI surfaces), we obtain the unit mass fields

$$\mathbf{M}_{(001)}^{(3,1)} = \frac{\mathbf{m}_{(001)}}{|\mathbf{m}_{(001)}|}, \quad \mathbf{M}_{(0\bar{1}0)}^{(3,1)} = \frac{\mathbf{m}_{(0\bar{1}0)}}{|\mathbf{m}_{(0\bar{1}0)}|}, \quad \mathbf{M}_{(\bar{1}00)}^{(3,1)} = \frac{\mathbf{m}_{(\bar{1}00)}}{|\mathbf{m}_{(\bar{1}00)}|}. \quad (\text{S5})$$

These values figure out a path which encloses the zero point, as shown in Fig. S1(b). Hence we have $w_1^{(1)} = w_{\text{I,V,VI}} = 1$ in the parameter space of enclosing this corner, implying that there are topological zero-energy states in this corner. Similarly, we can identify $w_1^{(1)}$ for the remaining corners, the completely results are shown in Fig. S1(b). Next, we determine the topological indexes of all edges. For example of the edge intersected by (100) and $(0\bar{1}0)$ surfaces (i.e., the edge in III and V surfaces), these effective mass fields contribute

$$\mathbf{M}_{(100)}^{(2,1)} = \frac{m_{1,(100)}}{|\mathbf{m}_{(100)}|}, \quad \mathbf{M}_{(0\bar{1}0)}^{(2,1)} = \frac{m_{1,(0\bar{1}0)}}{|\mathbf{m}_{(0\bar{1}0)}|}, \quad \mathbf{M}_{(100)}^{(2,2)} = \frac{m_{2,(100)}}{|\mathbf{m}_{(100)}|}, \quad \mathbf{M}_{(0\bar{1}0)}^{(2,2)} = \frac{m_{2,(0\bar{1}0)}}{|\mathbf{m}_{(0\bar{1}0)}|}. \quad (\text{S6})$$

These values in III and V surfaces figure out a path which cross the zero point, as shown in Fig. S1(b). Hence we have $C_0^{(1)} = C_{\text{III,V}} = 1$ and $C_0^{(2)} = C_{\text{III,V}} = 1$, i.e., $\mathbf{C}_{\text{III,V}} = (1,1)$, implying that there are topological zero-energy states in this edge. Similarly, we can identify $C_0^{(1),(2)}$ for the remaining edges, as shown in Fig. S1(b). Finally, the 3D inversion-symmetric HyOTI are determined, where the helical states are located at two edges along the z direction and the corner states are located at one corner of the other two edges; see Fig. S1(b). These results completely match with the OBC energy spectrum of $\mathcal{H}(\mathbf{k})$ in the main text.

We emphasize that this surface theory is also applicable to determine higher-order topological states. In the model (S1), the higher-order topological phases can be induced by adjusting the parameters. When taking $(B_1, B_2, B_3) = (0.35t_0, 0, 0.35t_0)$, we calculate the unit mass fields for all corners and edges, as shown in Fig. S2(a). It reveals a third-order topological phase with corner states. These corner states are located at the left (right) upper and left (right) lower of (001) [$(00\bar{1})$] surface. The OBC energy spectrum of $\mathcal{H}(\mathbf{k})$ further confirms these results. Moreover, we take

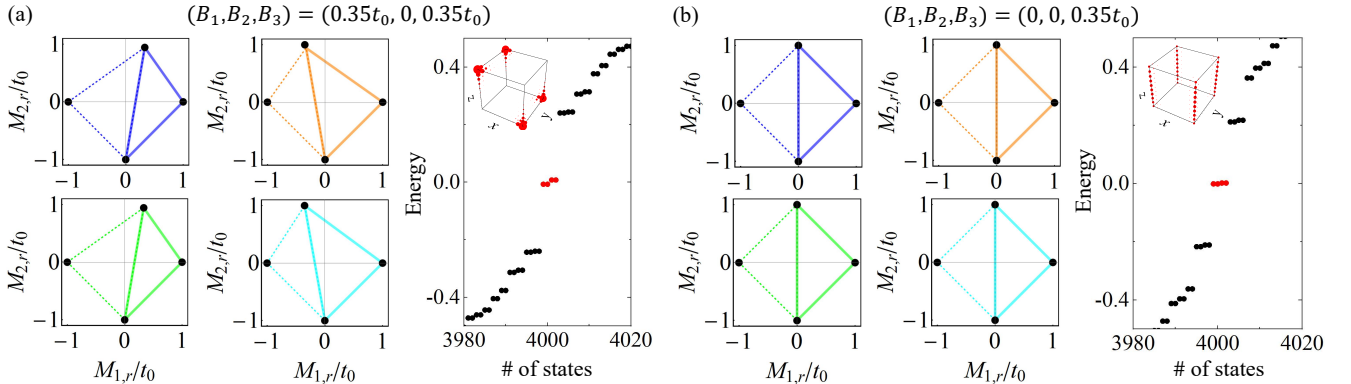


FIG. S2. Distribution of the unit mass fields enclosing 8 corners and 12 edges of (a) for $(B_1, B_2, B_3) = (0.35t_0, 0, 0.35t_0)$ and (b) for $(B_1, B_2, B_3) = (0, 0, 0.35t_0)$. The corresponding OBC energy spectrum gives four zero-energy states located in 4 corners for (a) and 4 hinges for (b). Here we take $m_0 = 5t_0$ and the lattice size is $N_x = N_y = N_z = 10$.

$(B_1, B_2, B_3) = (0, 0, 0.35t_0)$ to calculate the unit mass fields for all corners and edges, as shown in Fig. S2(b). It reveals a second-order topological phase with helical states, which are located at four edges along z direction. Similarly, the OBC energy spectrum of $\mathcal{H}(\mathbf{k})$ confirms these results. These results demonstrate that the surface theory is a powerful tool for determining the orders of the hybrid-order topology.

III. Circuit-based realization

We next show the expression of circuit Laplacian $\mathcal{J}(\omega)$ in detail. For the cubic circuit of Fig. 3 in the main text, the frequency-dependent Laplacian $\mathcal{J}(\omega)$ takes the form

$$\mathcal{J}(\omega) = \begin{bmatrix} j_{11} & j_{12} & j_{13} & j_{14} & j_{15} & 0 & 0 & 0 \\ j_{21} & j_{22} & j_{23} & j_{24} & 0 & j_{26} & 0 & 0 \\ j_{31} & j_{32} & j_{33} & j_{34} & 0 & 0 & j_{37} & 0 \\ j_{41} & j_{42} & j_{43} & j_{44} & 0 & 0 & 0 & j_{48} \\ -j_{15} & 0 & 0 & 0 & -j_{11} & -j_{12} & -j_{13} & -j_{14} \\ 0 & -j_{26} & 0 & 0 & -j_{21} & -j_{22} & -j_{23} & -j_{24} \\ 0 & 0 & -j_{37} & 0 & -j_{31} & -j_{32} & -j_{33} & -j_{34} \\ 0 & 0 & 0 & -j_{48} & -j_{41} & -j_{42} & -j_{43} & -j_{44} \end{bmatrix}. \quad (\text{S7})$$

The matrix elements are given by $j_{11} = -6\omega C_4 + \omega C_4 \sum_i \cos k_i - \omega C_B + iG_B - iG_{ii} - 1/(\omega L_g) + \omega C_{ii}$, $j_{12} = \omega C_B - iG_B$, $j_{13} = 2G_3 \sin k_3$, $j_{14} = 2G_1 \sin k_1 - 2i\omega C_2 \sin k_2$, $j_{15} = -2iG_5(\cos k_1 - \cos k_2)$. By carefully selecting the values of C_{ii} and G_{ii} , we obtain $j_{11} = \omega C_g - 1/(\omega L_g) + \omega C_4 \sum_i \cos k_i$, which can provide desired on-site potentials at given frequency ω_0 . Using the same design principles, the complete Hamiltonian for the inversion-symmetric HyOTI can be implemented. It is noted that the sign of the hoppings can be controlled by the directions of INIC and the signs of the capacitors [a negative capacitor is equivalent to an inductor because $i\omega C = -i/(\omega L)$ at $\omega = 1/\sqrt{LC}$].

IV. Tight-binding model in a 3D hexagonal lattice

We next provide a tight-binding model based on a 3D hexagonal lattice to realize the unconventional HyOTI with both helical and corner states. Firstly, we consider a tight-binding model $\mathcal{H}_{\text{Bi}}(\mathbf{k})$, which is topologically equivalent to a realistic model of bismuth [S59, S60]. It has three-fold rotation symmetry C_3^z and inversion symmetry \mathcal{I} and is defined on the 3D hexagonal lattice spanned by the lattice vectors $\mathbf{a}_1 = (1, 0, 0)$, $\mathbf{a}_2 = (-\frac{1}{2}, \frac{\sqrt{3}}{2}, 0)$ and $\mathbf{a}_3 = (0, 0, 1)$ [S66]. The corresponding Bloch Hamiltonian has 8 bands and is given by

$$\mathcal{H}_{\text{Bi}}(\mathbf{k}) = \begin{bmatrix} \mathcal{H}_{\text{I}}(\mathbf{k}) & \delta\mathcal{M}(\mathbf{k}) \\ \delta\mathcal{M}(\mathbf{k})^\dagger & \mathcal{H}_{\text{II}}(\mathbf{k}) \end{bmatrix}. \quad (\text{S8})$$

This Hamiltonian $\mathcal{H}_{\text{Bi}}(\mathbf{k})$ consists of two 3D topological insulators given by $\mathcal{H}_{\text{I}}(\mathbf{k})$ and $\mathcal{H}_{\text{II}}(\mathbf{k})$, which belong to the different C_3^z subspaces and are couple together via the mass matrix $\mathcal{M}(\mathbf{k})$ with the coupling strength δ . Moreover, we have

$$\begin{aligned} \mathcal{H}_{\text{I}}(\mathbf{k}) = & \Gamma_1 \{ m_{\text{I}}(1 + \cos \mathbf{k} \cdot \mathbf{a}_3) - t_{\text{I}}[\cos \mathbf{k} \cdot \mathbf{a}_1 + \cos \mathbf{k} \cdot \mathbf{a}_2 + \cos \mathbf{k} \cdot (\mathbf{a}_1 + \mathbf{a}_2)] \} \\ & + \lambda_{\text{I}}[\Gamma_2 \sin \mathbf{k} \cdot \mathbf{a}_1 + \Gamma_{2,1}^{\text{I},\text{I}} \sin \mathbf{k} \cdot \mathbf{a}_2 - \Gamma_{2,2}^{\text{I},\text{I}} \sin \mathbf{k} \cdot (\mathbf{a}_1 + \mathbf{a}_2) + \Gamma_3 \sin \mathbf{k} \cdot \mathbf{a}_3], \end{aligned} \quad (\text{S9})$$

$$\begin{aligned} \mathcal{H}_{\text{II}}(\mathbf{k}) = & \Gamma_1 \{ m_{\text{II}}(1 + \cos \mathbf{k} \cdot \mathbf{a}_3) - t_{\text{II}}[\cos \mathbf{k} \cdot \mathbf{a}_1 + \cos \mathbf{k} \cdot \mathbf{a}_2 + \cos \mathbf{k} \cdot (\mathbf{a}_1 + \mathbf{a}_2)] \} \\ & + \lambda_{\text{II}}[\Gamma_2 \sin \mathbf{k} \cdot \mathbf{a}_1 + \Gamma_{2,1}^{\text{II},\text{II}} \sin \mathbf{k} \cdot \mathbf{a}_2 - \Gamma_{2,2}^{\text{II},\text{II}} \sin \mathbf{k} \cdot (\mathbf{a}_1 + \mathbf{a}_2) + \Gamma_3 \sin \mathbf{k} \cdot \mathbf{a}_3] \\ & + \Gamma_4 \gamma_{\text{II}}[\sin \mathbf{k} \cdot (\mathbf{a}_1 + 2\mathbf{a}_2) + \sin \mathbf{k} \cdot (\mathbf{a}_1 - \mathbf{a}_2) - \sin \mathbf{k} \cdot (2\mathbf{a}_1 + \mathbf{a}_2)], \end{aligned} \quad (\text{S10})$$

$$\begin{aligned} \mathcal{M}(\mathbf{k}) = & \Gamma_2[\sin \mathbf{k} \cdot \mathbf{a}_1 + \sin \mathbf{k} \cdot (2\mathbf{a}_1 + \mathbf{a}_2)] + \Gamma_{2,1}^{\text{I},\text{II}}[\sin \mathbf{k} \cdot \mathbf{a}_2 + \sin \mathbf{k} \cdot (\mathbf{a}_2 - \mathbf{a}_1)] \\ & - \Gamma_{2,2}^{\text{I},\text{II}}[\sin \mathbf{k} \cdot (\mathbf{a}_1 + \mathbf{a}_2) + \sin \mathbf{k} \cdot (\mathbf{a}_1 + 2\mathbf{a}_2)] - i\Gamma_5[\cos \mathbf{k} \cdot \mathbf{a}_1 + \cos \mathbf{k} \cdot (2\mathbf{a}_1 + \mathbf{a}_2)] \\ & - i\Gamma_{5,1}^{\text{I},\text{II}}[\cos \mathbf{k} \cdot \mathbf{a}_2 + \cos \mathbf{k} \cdot (\mathbf{a}_2 - \mathbf{a}_1)] - i\Gamma_{5,2}^{\text{I},\text{II}}[\cos \mathbf{k} \cdot (\mathbf{a}_1 + \mathbf{a}_2) + \cos \mathbf{k} \cdot (\mathbf{a}_1 + 2\mathbf{a}_2)], \end{aligned} \quad (\text{S11})$$

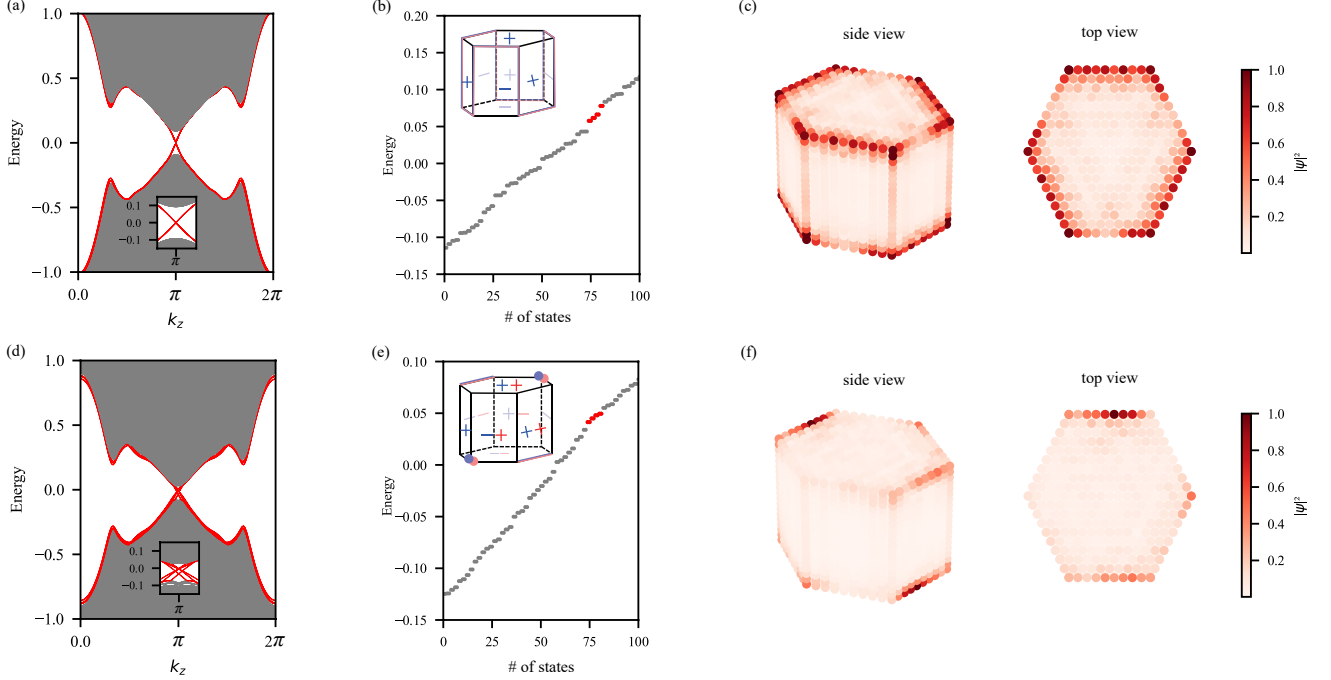


FIG. S3. Numerical results of the tight-binding Hamiltonian $\mathcal{H}_{\text{TB}}(\mathbf{k})$ on a hexagonal geometry. The k_z -resolved energy spectrum (a) without and (d) with additional mass terms, where the system size is 52×52 . The insets give the details of energy bands near $k_z = \pi$, where we take the system size as 72×72 . The 100 eigenstates near the Fermi level are plotted by taking the completely OBCs, where two insets illustrate the signs of effective surface masses, respectively. Here we take the system size as $20 \times 20 \times 20$. The corresponding real-space contributions of the states with red color are shown in (c) and (f), respectively. Both side and top views show a second-order topological phase for (c) and a unconventional hybrid-order (coexistence of helical and corner states) topological phase for (f).

where $\Gamma_1 = \tau_3\sigma_0, \Gamma_2 = \tau_1\sigma_1, \Gamma_3 = \tau_2\sigma_0, \Gamma_4 = \tau_1\sigma_2, \Gamma_5 = \tau_3\sigma_1$, and $\Gamma_{\mu,\nu}^{i,j} = (C_{3,i}^z)^{\nu}\Gamma_{\mu}(C_{3,j}^z)^{-\nu}$. Here we have $\mu \in \{1, \dots, 5\}$, $i, j \in \{\text{I,II}\}$, $\nu \in \{1, 2\}$, $C_{3,\text{I}}^z = \tau_0 e^{i\frac{\pi}{3}\sigma_3}$, and $C_{3,\text{II}}^z = -\tau_0\sigma_0$, so that the threefold rotation symmetry is given by $C_3^z = C_{3,\text{I}}^z \oplus C_{3,\text{II}}^z$. It is noted that the Pauli matrices σ_i and τ_i denote the freedom degree of spin and orbit, respectively. By taking the parameter $m_{\text{I}} = m_{\text{II}} = 2.0$, $t_{\text{I}} = t_{\text{II}} = 1.0$, $\lambda_{\text{I}} = 0.3$, $\lambda_{\text{II}} = \gamma_{\text{II}} = 1.0$, and $\delta = 0.3$, we obtain the k_z -resolved energy spectrum in Fig. S3(a). There are six Kramers pairs in the gapless helical states [see the inset of Fig. S3(a)], implying that there are helical states in the 6 edges of the 3D hexagonal geometry. Further, we take the OBCs along all directions and obtain its energy spectrum, of which 100 states near the Fermi level are plotted in Fig. S3(b). The real-space contributions of 8 states marked as red color are shown in Fig. S3(c), confirming the second-order topological phases with helical modes. Such topological states can be understood through the picture of mass domain wall induced by the effective surface masses; see the inset of Fig. S3(b).

Next, we introduce two additional mass terms $m_{x,z}$ into the tight-binding model of bismuth. The total Hamiltonian is given by

$$\mathcal{H}_{\text{TB}}(\mathbf{k}) = \mathcal{H}_{\text{Bi}}(\mathbf{k}) + \mathcal{H}_{\text{m}}(\mathbf{k}), \quad \mathcal{H}_{\text{m}}(\mathbf{k}) = \begin{pmatrix} m_z\tau_0\sigma_0 & m_x\tau_0\sigma_0 \\ m_x\tau_0\sigma_0 & -m_z\tau_0\sigma_0 \end{pmatrix}. \quad (\text{S12})$$

As a result, these helical states along z direction open a energy gap through the nonzero $m_{x,z}$. By taking the parameters $m_z = -0.05$ and $m_x = -0.15$, it is seen that the degeneracy of six Kramers pairs are broken in Fig. S3(d). Meanwhile, a very small band gap emerge; see the inset of Fig. S3(d). Since $m_{x,z}$ provide the additional surface masses, the effective mass fields are changed into the forms of the inset of Fig. S3(e). Applying the proposed surface theory, we immediately determine that the system has the coexistence of 0D corner states and 1D edge states. The OBC energy spectrum in Figs. S3(e) and S3(f) confirm these results.